



HAL
open science

High-frequency wall heat flux measurement during wall impingement of a diffusion flame

Julien Moussou, Guillaume Pilla, Julien Sotton, Marc Bellenoue, Fabien Rabeau

► **To cite this version:**

Julien Moussou, Guillaume Pilla, Julien Sotton, Marc Bellenoue, Fabien Rabeau. High-frequency wall heat flux measurement during wall impingement of a diffusion flame. *International Journal of Engine Research*, 2021, 22 (3), pp.847-855. 10.1177/1468087419878040 . hal-03169234

HAL Id: hal-03169234

<https://ifp.hal.science/hal-03169234>

Submitted on 15 Mar 2021

HAL is a multi-disciplinary open access archive for the deposit and dissemination of scientific research documents, whether they are published or not. The documents may come from teaching and research institutions in France or abroad, or from public or private research centers.

L'archive ouverte pluridisciplinaire **HAL**, est destinée au dépôt et à la diffusion de documents scientifiques de niveau recherche, publiés ou non, émanant des établissements d'enseignement et de recherche français ou étrangers, des laboratoires publics ou privés.

High-frequency wall heat flux measurement during wall impingement of a diffusion flame

Julien Moussou^{1,2} , Guillaume Pilla¹, Julien Sotton², Marc Bellenoue² and Fabien Rabeau¹

Abstract

The efficiency of internal combustion engines is limited by heat losses to the wall of the combustion chamber. A precise characterization of wall heat flux is therefore needed to optimize engine parameters. However, the existing measurements of wall heat fluxes have significant limitations; time resolution is often higher than the timescales of the physical phenomena of flame–wall interaction. Furthermore, few studies have investigated diesel flame conditions (as opposed to propagation flames). In this study, the heat flux generated by a diffusion flame impinging on a wall was measured with thin-junction thermocouple, with a time resolution of the whole acquisition chain better than 0.1 ms. The effects of variations in ambient gas temperature, injection pressure and injector–wall distance were investigated. Diesel spray impingement on the wall is shown to cause strong gas–wall thermal exchange, with convection coefficients of 6–12 kW/m²/K. Those results suggest the necessity of close-wall aerodynamic measurements to link macroscopic characteristics of the spray (injection pressure, impingement geometry) to turbulence values.

Keywords

Diesel combustion, heat flux, high-frequency measurement, convection coefficient

Introduction

Internal combustion (IC) is forecasted to remain a major source of energy and be present in the majority of automobile engines in the next decades.^{1,2} Growing concerns about emissions of CO₂ and pollutants demand further increases in efficiency. Heat transfer losses are around 10%–40% of the total fuel energy, depending on engine operating point and conditions,^{3–5} and thus are a major source of inefficiency; future efficiency targets can only be met by reducing wall heat transfer losses over an engine cycle. It is therefore necessary to accurately determine heat losses during each phase of the combustion cycle, in order to identify guidelines for the future optimization of engine operating parameters. Because the highest heat fluxes are found during the combustion event, that phase of the combustion cycle is the focus of this study.

In order to replicate combustion in engine conditions, multiple configurations have been used: constant volume combustion chamber (CVCC),⁶ rapid compression machine (RCM)⁷ or instrumented IC engines.⁸ CVCC and RCM enable easy sensor access to the combustion chamber while maintaining conditions similar to IC engines.

Because heat transfers vary significantly during the engine cycle, accurate information can only be obtained with in-cycle thermal measurements, which requires temporal resolutions of the millisecond or less. For instance, at an engine speed of 1200 r/min, temporal resolution to the crankshaft angle degree (°CA) corresponds to a time resolution of 0.15 ms or a cutoff frequency of 7.2 kHz. This proves challenging because of thermal inertia effects in standard sensors.

Multiple diagnostics have been used to measure in-cycle thermal information on the surface of the combustion chamber, in particular thermocouples,^{8,9} resistance temperature detectors (RTD),^{10,11} thermopiles,^{12–14} laser-induced phosphorescence (LIP)^{15,16} and infrared

¹IFP Énergies nouvelles, Institut Carnot IFPEN Transports Energie, Rueil-Malmaison, France

²Institut PPRIME, CNRS/ ISAE-ENSMA /Université de Poitiers, Chasseneuil du Poitou, France

Corresponding author:

Guillaume Pilla, IFP Énergies nouvelles, 1-4 avenue du Bois Préau, 92852 Rueil-Malmaison, France.

Email: guillaume.pilla@ifpen.fr

thermometry.^{15,17} The most common is thin-junction thermocouple and is the one used here; as with every other method but thermopiles, a surface temperature is measured, which allows us to recover heat flux via a mathematical model. Thermopiles provide direct heat flux information with minimal data processing, but require a large surface area (causing significant spatial averaging) and have larger response times than other methods.^{11,12,14} Few RTD sensors exist, none of them commercially available, although recent developments suggest that the technology can be as accurate as thermocouples.¹⁰ LIP and infrared thermometers use emissions from heated body or activated phosphors and are difficult to apply in compression-ignition (CI) conditions due to interference between the optical signal and soot radiation.^{17–19} Further comparisons of the methods of heat flux measurement can be found in the literature.^{11,20}

Previous studies on premixed flames for spark-ignition (SI) engines show the main features of transient heat flux curves.^{6,7,21,22} The heat flux first increases in a fraction of millisecond from zero to a few MW/m² and decreases in about the same time. That heat flux spike is attributed to flame wall interaction (FWI) processes: the hot flame front, close to the adiabatic flame temperature, approaches the wall until heat losses cause flame quenching.

In CI engines, the combustion phenomena are different (spray mixing, diffusion flame).²³ Heat flux measurements therefore yield different features,^{8,9,24} with heat fluxes as high as 10 MW/m² exhibiting a plateau of a few milliseconds rather than a spike of heat flux.^{25,26} Extensive studies^{27–29} about diesel jet impingement showed that a cool flame develops close to the wall, due to either higher premixing or because of extinction of the diffusion flame or dying flame, although it is still surrounded by high temperature reactions at the diverted tip, in some cases leading to the deposition of soot.^{27,28} Thermal transfer during jet impingement is not understood as well as in SI engines.

In this study, a high-frequency thermocouple measurement of wall temperature is made during spray impingement in a CVCC. Variations are performed on injection pressure, injector-wall distance and ambient gas temperature. The highly resolved temperature measurements (temporal resolution better than 0.15 ms) allow us to capture the characteristics of each heat flux curve throughout the combustion, without the need for ensemble averages of data. The scales of rise of heat flux in time and maximum flux are analyzed and compared with relevant phenomenological observations. That experiment also highlights the capabilities of that new experimental setup for further study.

Methods

Combustion environment

Experiments were conducted using a high temperature high pressure chamber, later-on referred to as constant

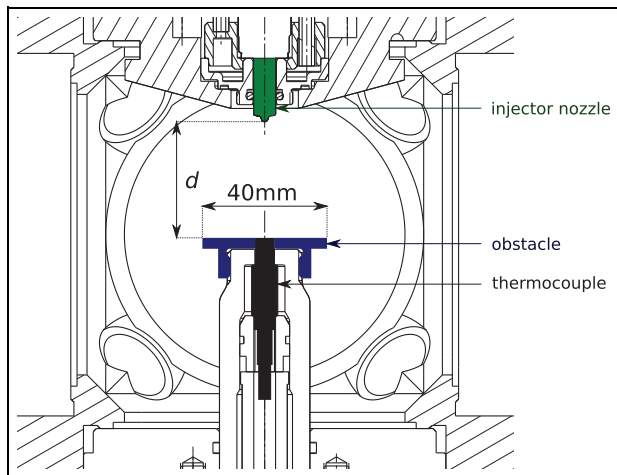


Figure 1. CV chamber with obstacle and thermocouple schematics.

volume (CV) chamber. This chamber, previously described in the literature,³⁰ aims at creating thermodynamic conditions close to engines, with pressures up to 150 bar and temperatures up to 1500 K. To achieve this, the CV chamber is initially preheated at 465 K. A premixed, lean inflammable mixture with fan-induced turbulence is then ignited by spark plugs, causing a pre-combustion phase of less than 100 ms that greatly increases gas temperature and pressure inside the chamber. In the following few seconds, pressure and temperature of chamber gases decrease due to cooling via wall heat losses. Finally, a direct fuel injection can be synchronized to a target pressure and temperature during the cooling process within a 1% reproducible precision. Depending on the final mixture composition after the precombustion event, the fuel spray can autoignite.

A pressure sensor (AVL GU21D) monitors the instantaneous pressure inside the CV chamber. The CV chamber is also equipped with sapphire windows allowing optical access across the chamber volume. Imaging of the spray and the combustion can therefore be performed. In this study, a Schlieren imaging technique was applied perpendicularly to the injection axis allowing us to capture qualitative spray shape information.

The experimental setup is shown in Figure 1. A flat obstacle is placed inside the combustion chamber as to simulate jet impingement on a wall. The obstacle, a 40-mm diameter stainless steel (APX4) disk, is placed perpendicular to the injection axis and aligned with it. A thermocouple is flush mounted at its center for thermal measurements described later. The insertion system is such that the distance d between the injector nozzle and the obstacle can be adjusted.

Experimental conditions

A single-hole injector was used (Bosch common rail solenoid, 90- μ m nozzle outlet diameter, ECN #13) with

Table 1. Operating conditions through parametric variations.

	Ambient gas temperature T_a , K	Injection pressure P_{inj} , bar	Wall/injector distance d , mm
Reference condition	850 ± 10	1500 ± 10	45 ± 0.5
Temperature variation	966 ± 10	1500 ± 10	45 ± 0.5
	780 ± 10	1500 ± 10	45 ± 0.5
Injection pressure variation	850 ± 10	1000 ± 10	45 ± 0.5
	850 ± 10	500 ± 10	45 ± 0.5
Distance variation	850 ± 10	1500 ± 10	60 ± 0.5
	850 ± 10	1500 ± 10	80 ± 0.5

Gas composition and density before injection are always the same (15% O₂ + 75.2% N₂ + 6.2% CO₂ + 3.6% H₂O, 23.5 ± 0.3 kg/m³).

pure *n*-dodecane as fuel. A single injection of 1.5 ms duration was performed, giving an injected mass of 3.6 ± 0.1 mg for an injection pressure of 1500 bar.

Thermodynamic conditions in which the spray was injected in the CV chamber were taken close to the ECN spray A temperature and density targets.³⁰ A reference point was chosen from which injection pressure, ambient gas temperature at injection and distance between injector nozzle and obstacle were varied one at a time. The experimental conditions are given in Table 1. Each experimental condition was repeated at least five times to allow statistical analysis of the data.

Due to the large volume of the combustion chamber (1.4 L), the global air/fuel ratio in the chamber is very high (above 100). Transient pressure recordings with a resolution below 0.5 bar show no impact of the diesel combustion on chamber pressure.

Gas composition at the start of injection is equivalent to that found in engines for 25% (molar) exhaust gas recirculation.

Thermal measurements

The temperature inside the CV chamber was held constant for a sufficient long time before the precombustion to assume that heat flux is zero before this event; temperature before the precombustion is always in the 465–475 K range. The wall temperature (as recorded by the thermocouple) is about 25–35 K higher at the start of injection than before precombustion. Finally, during the injection event, wall temperature increases by 5–20 K. All those temperature changes are estimated to have a negligible effect on the thermal properties of the wall.

It is also assumed that heat conduction is monodimensional (normal to the wall). That assumption can be justified by a Fourier number analysis: as the duration of the heat transfer event during and after injection is 10 ms or less, heat diffusion distances in the thermocouple at the relevant timescales are about 0.1 mm, whereas both the expected spatial inhomogeneities of the incident flux and the geometry of the thermocouple have characteristic sizes of about 1 mm. In these conditions, the mathematical problem of thermal diffusion

can be solved analytically. Indeed, the measurement of wall temperature is sufficient to compute the heat flux using³¹

$$q(t) = \sqrt{\frac{k\rho C_p}{\pi}} \int_{t'=-\infty}^t \frac{\partial T_w}{\partial t} \frac{dt'}{\sqrt{t-t'}} \quad (1)$$

where $q(t)$ is the transient heat flux in W/m², $\sqrt{k\rho C_p}$ is the thermal effusivity of the thermocouple junction material (chromel) and T_w is the measured wall temperature in K. The manufacturer's specification $\sqrt{k\rho C_p} = 8430 \text{ W}\cdot\text{s}^{0.5}\cdot\text{m}^{-2}\cdot\text{K}^{-1}$ was used for the effusivity value.

The starting point for the integral is chosen before the precombustion event. Although significant heat fluxes are calculated during precombustion itself (2–3 MW/m²), it decreases down to about 0.05 MW/m² (below the measurement resolution) in about 500 ms, well before the injection event; therefore, no background flux subtraction is necessary.

Wall temperature on the obstacle was measured similarly to previous studies³²: the output of a K-type thin junction thermocouple (Medtherm TCS-244-KU(KU-156)-72-11340) is amplified by a custom electronic card (Analog device AD595 with 10-kHz low-pass filter) whose output is recorded with an oscilloscope (Lecroy Waverunner 610Zi). Before differentiation, the temperature trace is smoothed using a Tikhonov regularization, which is more adapted to temperature-to-flux reconstruction problems than linear low-pass filtering,³³ using a ready-made MATLAB script.³⁴

Precision on the final flux measurement is estimated to be better than 0.1 MW/m² based on the noise obtained on the heat flux measurement during the precombustion event.

The response time of the whole processing chain (thermocouple, amplifier, recording and processing code) has been measured using a laser heating setup similar to that of previous literature.³⁵ Imposing a step of heat flux (rise time < 1 μs, duration 8 ms) on the thermocouple junction causes a non-instantaneous increase in the reconstructed heat flux, whose rise time gives an estimation of the time resolution of the whole processing chain. The response time of the whole setup was measured to be 0.08–0.1 ms, which is compatible with an engine target of 1 °CA at 1200 r/min.

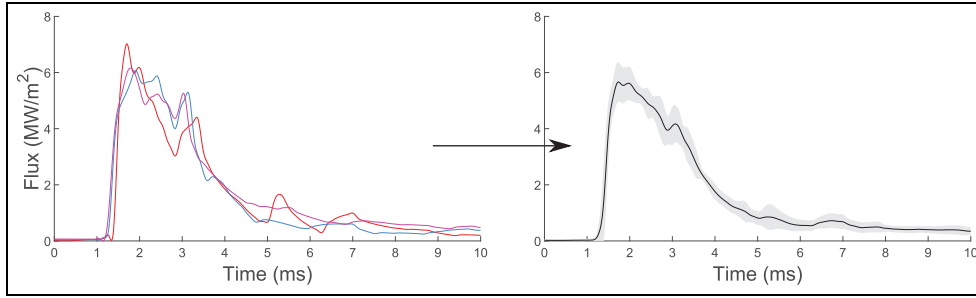


Figure 2. Result post-processing for reference case ($T_a = 850$ K, $P_{inj} = 1500$ bar, $d = 45$ mm). Left: heat flux traces for three typical repetitions of the experiment. Right: point-by-point average and standard deviation of all ($N = 7$) repetitions.

General shape and statistical processing

Figure 2 shows the general shape of the results obtained for three repetitions of the reference point ($P_{inj} = 1500$ bar, $d = 45$ mm, $T_a = 850$ K). Time is counted starting from the electronic command of injection.

Defining the start of heat flux as the timing at which the flux value is above 0.5 MW/m², the jet impinges on the wall with a delay of about 1.5 ms after the start of injection. This delay is attributed to the hydraulic delay of the injector (about 0.3 ms) and to the travel time between the nozzle and the obstacle. The heat flux then increases in less than 0.5 ms up to values of the order of 5 MW/m². Finally, it decreases back to zero in a few milliseconds.

The steep initial gradient in heat flux is reproducible for each shot: both the timing of the start of heat flux and the rise time (duration between the start of heat flux and 63% of heat flux maximum) exhibit standard deviations of about 0.06 ms. However, these curves exhibit shot to shot variations in later stages. Peaks and valleys of about 2 MW/m² amplitude are observed. Those are attributed to physical changes in the heat flux due to statistical variations in the jet/wall interaction. To obtain quantitative measurements, such random deviations are filtered by point-by-point averaging of repetitions of the same operating condition. Figure 2 shows the resulting mean as a continuous line and the standard deviation as the shaded area surrounding it.

Results and discussion

Radiative heat flux estimation

Testing radiative heat transfer. In this study, convective and radiative transfers are considered predominant to describe heat transfer to the wall. Therefore, conduction will not be further discussed. These two modes of heat transfer tend to happen simultaneously because they are both correlated with jet impingement: convective transfer happens only if hot gases are close to the wall, and radiative transfer is maximal when soot are close to the wall. According to literature,³⁶ soot in diesel flames can emit more than 1 MW/m² of blackbody

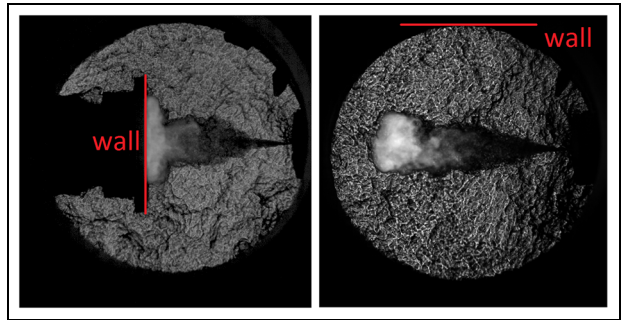


Figure 3. Schlieren imaging of the combustion. Left: jet impingement at a distance of 45 mm. Right: radiation test: the obstacle and heat flux sensor are placed away from the jet, and there is no impingement.

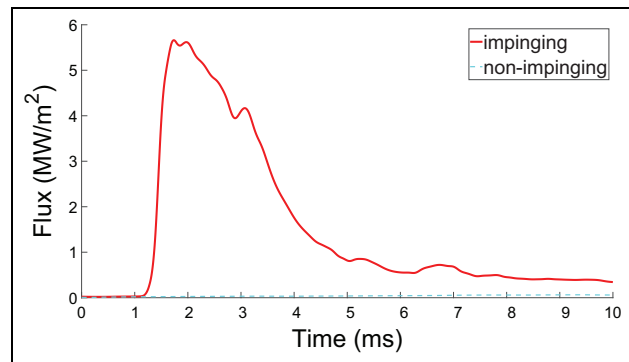


Figure 4. Heat flux for impinging and non-impinging case.

radiation heat flux. Therefore, a specific experiment was designed to evaluate the contribution of the radiative component to the overall heat flux transmitted to the wall. As shown in Figure 3, the reference test case (left) was compared to a case where the wall is 45 mm from the flame (right). In this configuration, the wall only sees radiation from soot, and heat from convection or conduction is considered negligible. Schlieren imaging presented in Figure 3 clearly shows the incandescent soot radiation at the tip of the jet.

Results of that test are shown in Figure 4. For the non-impinging case, heat flux in the 10 ms following the injection command is inferior to 0.05 MW/m², below the estimated precision limit of 0.1 MW/m². There is no

statistically significant difference between heat flux traces during that time and in the 10 ms immediately preceding injection either. Therefore, the maximum radiative heat flux will be considered to be 0.1 MW/m^2 .

Estimation of the maximum radiative heat flux inside the flame. In the previous experimental test case, radiating soot particles are far away from the sensor, which reduces the incident radiative heat flux compared to the reference case where soot is very close (impinging jet). That geometrical effect can be evaluated by an elementary solid angle calculation. Soot emission is modeled as a disk of radius R whose surface area emits uniform and isotropic radiation from a distance d of the sensor. It is furthermore assumed that there is no optical absorption in the transmitting medium. Under those assumptions, the radiative heat flux received at the sensor location is found to be proportional to the geometrical factor

$$G = 1 - \frac{1}{\sqrt{1 + \left(\frac{R}{d}\right)^2}} \quad (2)$$

When the sensor is close to the emitting area ($d \ll R$), the received radiation is equal to the emission ($G = 1$); further away, it is only a fraction of the emission. In the previous test case, $d = 45 \text{ mm}$ is taken from the distance between the injection axis and the sensor. The image from Figure 3, right allows us to evaluate $R = 20 \pm 10 \text{ mm}$ based on the glowing area, where the large uncertainty takes into account that soot radiation is out of focus for Schlieren imaging; that estimate of soot cloud size is compatible with data from previous experimental studies using formaldehyde laser-induced fluorescence or soot extinction diagnostics.^{27,37} The corresponding G is therefore estimated between 0.09 and 0.25.

This calculation leads to the estimation of a maximum radiative heat transfer component of 0.6 MW/m^2 . That value is about 10% of the observed peak of heat flux during jet impingement. Convective effects are then the dominant effect of heat transfer in the present experiments and will be the focus of the following analysis.

Ambient gas temperature variation

The ambient gas temperature at which the injection is performed can be adjusted by changing the timing of injection. Figure 5 shows the effect of that variation on the measured heat flux for three temperatures: 966, 850 and 780 K.

As the ambient gas temperature is increased, the heat flux peaks sooner: the delay between injection and heat flux peak increases from 1.36 to 1.63 ms (jitter is of the order of 0.05 ms, i.e. negligible). This is due to earlier spray impingement, as combustion causes gas expansion which increases spray tip speed. That effect increases with higher temperature.³⁸ With increasing

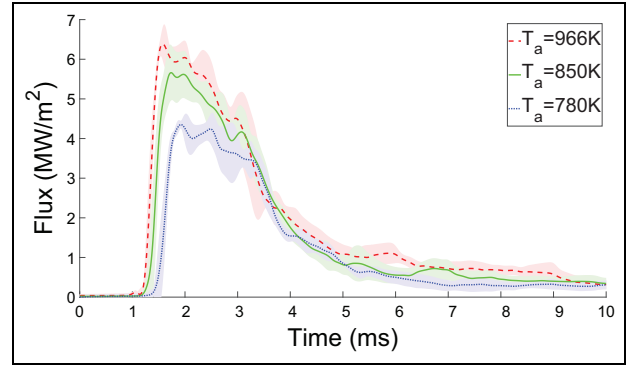


Figure 5. Heat fluxes measured for three different ambient gas temperatures ($P_{inj} = 1500 \text{ bar}$, $d = 45 \text{ mm}$ in all cases).

ambient temperature, an increase in heat flux is observed as well, as the peak value varies from 4.4 ± 1.0 to $6.4 \pm 0.4 \text{ MW/m}^2$.

In order to analyze that increase, recall Newton's law of convection

$$Q = h(T_g - T_w) \quad (3)$$

where Q is the local heat flux in W/m^2 ; h is the convection coefficient in $\text{W/m}^2/\text{K}$; T_g , T_w are, respectively, the gas and wall temperature in K.

The following analysis aims to determine estimates of the unknown quantities (h , T_g) in Newton's law (cf. equation (3)) using the experimental determination of wall temperature T_w (by thermocouple measurements), heat flux Q (cf. equation (1)), and the ambient gas temperature T_a (computed from pressure sensor data).

While ambient gas temperature does have an effect on spray tip speed due to autoignition delay effects, when the spray tip penetration reaches 45 mm, spray tip speed is the same for every temperature.³⁸ Therefore, turbulence inside the center line of the jet is assumed to be identical after jet impingement for the different ambient temperatures. If so, the convection coefficient h is constant with ambient gas temperature, although it may vary with time. T_w is measured and shows very low variations in time, within 5 K, compared to gas temperature exhibiting variations in the order of 200 K. As a result, the observed increase in heat flux must be linked with an increase in T_g .

Let $\delta T = T_g - T_a$ be the difference in temperature between gases next to the sensor and those in the bulk of the CV chamber. Assuming as a first-order approximation that δT is independent of the ambient gas temperature, it follows that

$$Q = h(T_a + \delta T - T_w) \quad (4)$$

where Q , T_a , T_w are known experimentally and h , δT do not vary as T_a is varied.

Under those hypotheses, the values of h , δT can be recovered by fitting the experimental data, as shown in Figure 6. A least-square fit weighted by the inverse of standard deviations observed on the experimental data

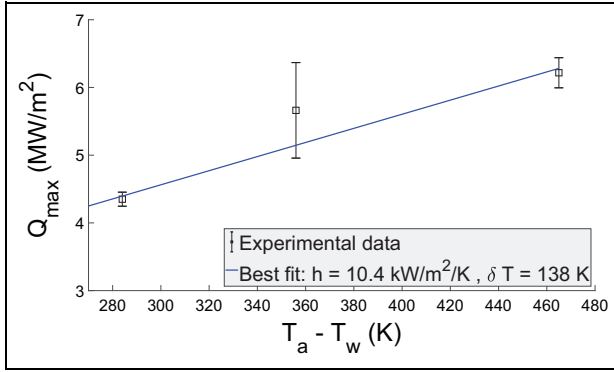


Figure 6. Flux versus temperature difference for the temperature variation.

Experimental data show the peak of flux. Convection coefficient and increase in temperature are extracted from a weighted mean squares fit. Fit coefficient values are given with more digits than physically significant (uncertainty estimated to be 10%–15%).

was applied on values from the peak of heat flux and yields $h = 10 \text{ kW/m}^2/\text{K}$ and $\delta T = 140 \text{ K}$. The fitting uncertainty on these values is estimated to be about 10%–15%.

The convection coefficient value of $h \sim 10 \text{ kW/m}^2/\text{K}$ is two to five times higher than those obtained by previous experimental²⁴ or correlation-based³⁹ studies. Most likely that is due to differences in the experimental setup (engine instead of CV chamber cases). In particular, a global pressure increase in the chamber during combustion, as observed in engines, might have an effect on turbulence and hence the convection coefficient, whereas in this study, no such increase occurs (due to the very small global air/fuel ratio) and the combustion occurs at constant pressure. Furthermore, correlation-based studies involve considerable spatial averaging (as heat coefficient correlations were calibrated from cylinder-averaged data), and previous experimental studies have usually lower bandwidths (either because of acquisition chain or post-processing effects) than the 10 kHz effective acquisition frequency reported here. That causes heat flux peaks to be underestimated in those previous studies and explains lower values of h .

The temperature increase of 140 K can be compared with non-impinging jet data. A reactive spray model from the literature⁴⁰ yields an fuel/air ratio = 3.75 in the center line of a non-impinging dodecane jet at a distance of 45 mm. Assuming adiabatic constant-pressure complete reactions, such an air–fuel ratio would cause an increase in temperature of about 600 K.⁴¹ The discrepancy between that value and the observed 140 K can be explained by a higher fuel/air ratio in the impinging jet case than for a non-impinging jet or by non-complete reactions.

Injection pressure variation

Figure 7 shows the effect of varying the injection pressure. At higher injection pressure, the jet is faster and

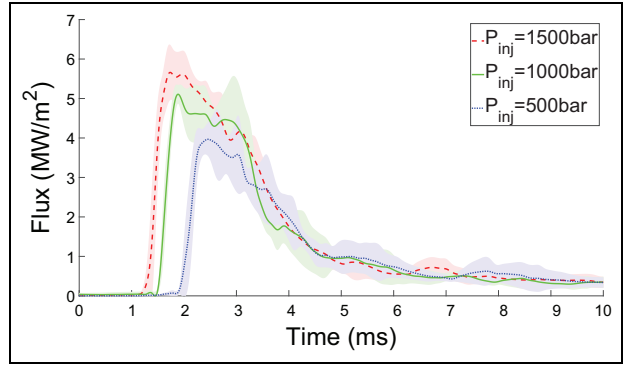


Figure 7. Injection pressure variation ($T_a = 850 \text{ K}$, $d = 45 \text{ mm}$ in all cases).

hence impinges sooner on the wall (delay between injection and heat flux start goes from 1.5 to 2.1 ms between 1500 and 500 bar of injection pressure). Heat flux is also higher: it peaks from $5.7 \pm 0.7 \text{ MW/m}^2$ at 1500 bar versus $4.0 \pm 0.4 \text{ MW/m}^2$ at 500 bar.

Jet speed and therefore entrained air turbulence increase as the injection pressure increases, and it is expected that this causes a significant change in the convection coefficient. Assuming that effect is the main reason for the heat flux increase observed in Figure 7 as injection pressure increases, the variation in gas temperature close to the sensor is neglected. Using the value of $\delta T = 140 \text{ K}$ obtained above, convection coefficients can be computed for every injection pressure.

The results are shown in Figure 8. The convection coefficient increases by about 50% between the extremes of injection (from 500 to 1500 bar). The impingement speed of the jet can be estimated from the literature model used previously⁴⁰; the velocity at 45 mm of the nozzle on the center line of a steady-state free (non-impinging) jet is 52 m/s at 500 bar and 94 m/s at 1500 bar, an increase by 80%.

Distance variation

The distance between the injector nozzle and the obstacle was varied between 45 and 80 mm (cf. Table 1). Figure 9 shows the results obtained measuring the

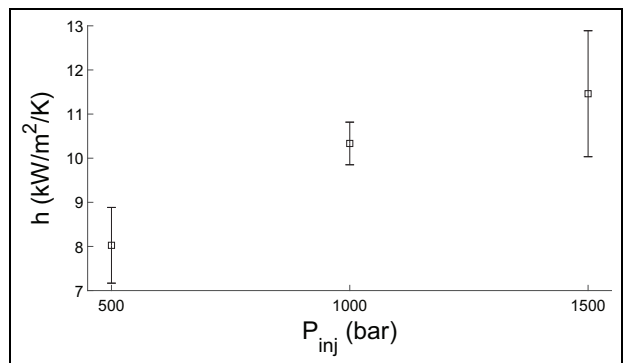


Figure 8. Convection coefficient variation with injection pressure.

heat flux in those different conditions. When that distance is higher, jet impingement occurs later which explains the later arrival timing (up to 3.1 ms for the larger distance) and some jitter (flux peak arrival has 0.15 ms of standard deviation, leading to a slower slope in the averaged curve) for the larger distance $d = 80$ mm.

A change in distance between the injector and the obstacle has two effects on the physics of the impingement process. On one hand, turbulence is lower further away from the nozzle, hence the convection coefficient is expected to be lower further downstream. On the other hand, higher mixing with fresh gases means the fuel/air ratio is lower, hence closer to stoichiometry, and gas temperature might be increased due to a higher release of energy by rich combustion reactions.

To deal with the gas temperature change, it can be assumed as a first-order approximation that the actual temperature increase δT for a given case of wall/injector distance is proportional to the temperature increase computed for a homogeneous, adiabatic, constant-pressure, complete reaction with the fuel/air ratio for a free jet. The reacting-jet model cited previously³⁸ predicts equivalence ratios of $\phi = 3.75$ at 45 mm and $\phi = 2.01$ at 80 mm for a free jet. The actual temperature increase in the 45 mm case is known from the aforementioned analysis of ambient temperature variations.

The convection coefficient can then be recovered by a similar procedure as previously and are shown versus the obstacle impact velocity in Figure 10. The convection coefficient decreases when the wall/injector distance is increased, from 11.5 to 6.5 kW/m²/K.

The previously cited reactive spray model from the literature⁴⁰ yields a velocity of 94 m/s at 45 mm and 54 m/s at 80 mm of the nozzle (on the center line of a steady-state free jet). Spray velocity is very similar in the (1500 bar, 80 mm) case as in the (500 bar, 45 mm) case (54 vs 52 m/s); nonetheless, the convection coefficient is lower in the higher-distance case (6.5 vs 8 kW/m²/K). Assuming that the estimation of the impingement velocity from a steady-state free jet model is roughly correct, this shows that the impingement

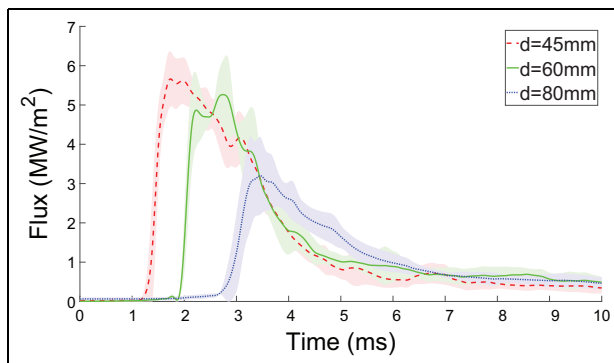


Figure 9. Nozzle-obstacle distance variation ($T_a = 850$ K, $P_{inj} = 1500$ bar in all cases).

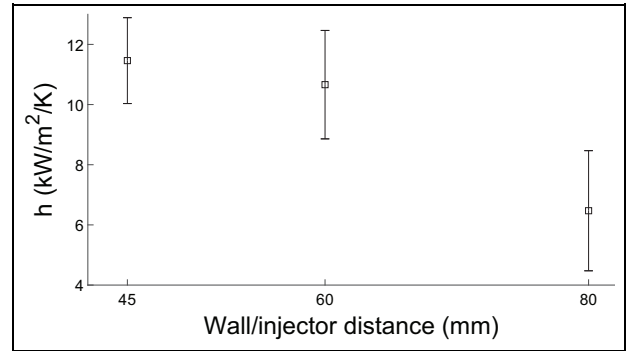


Figure 10. Convection coefficient variation with wall/injector distance.

velocity is not an adequate representation of the aerodynamic phenomena at hand. Indeed, the convection coefficient is driven by small-scale turbulence, whose intensity is not well correlated with that of large-scale advection motion.

Conclusion

Transient heat flux transfer by an impinging diesel jet was measured in the reference conditions of the ECN spray A, with variations in ambient gas temperature, injection pressure and distance between the injection and the obstacle it impinges on.

The high temporal resolution of the acquisition chain allows us to observe variations in the heat flux during the injection process. Reaching time resolutions better than the symbolic target of 1 °CA at 1200 r/min (0.15 ms) constitutes an improvement over previous studies of CI engines. It is nonetheless likely that the rise in heat flux is not fully resolved, and further improvements in temporal resolution would be desirable: data show rise times of about 0.3 ms, close to the temporal resolution.

Under simple assumptions of gas temperature next to the sensor location, convection coefficient values can be recovered and range from 6 to 12 kW/m²/K as the jet interacts with the wall. Values of heat flux peaks and associated convection coefficients are somewhat higher than previous studies for diesel jets, which can be attributed to sharper heat flux determination thanks to the better measurement resolution. Such values are also one order of magnitude higher than observed in SI engines, due to the high turbulence induced by spray injection.

In future work, simultaneous and near-wall gas temperature and flux measurements would remove the need for first-order interpretation hypotheses about near-wall gas temperature. Characterizing turbulence levels next to the wall under the same parametric variations would allow us to link microscopic turbulence processes to the macroscopically observed convection coefficient. Non-reactive jets might also be used in order to decouple induced turbulence effects and temperature effects.

Acknowledgements

The author(s) acknowledge the assistance of Clément Bramouille and Thomas Collazo for data collection.

Declaration of conflicting interests

The author(s) declared no potential conflicts of interest with respect to the research, authorship and/or publication of this article.

Funding

The author(s) received no financial support for the research, authorship and/or publication of this article.

ORCID iD

Julien Moussou  <https://orcid.org/0000-0003-4973-8201>

References

1. Scharf J, Ogrzewalla J, Wolff K, Uhlmann T, Thewes M, Balazs A, et al. Gasoline engines for hybrid powertrains: high tech or low cost? *FEV white paper* 2017, <https://www.fev.com/en/press/whitepapers/high-tech-or-low-cost.html>
2. Meszler D, German J, Mock P and Bandivadekar A. CO₂ reduction technologies for the European car and van fleet: a 2025–2030 assessment, 2017, <https://theicc-t.org/publications/co2-reduction-technologies-european-car-and-van-fleet-2025-2030-assessment>
3. Holmberg K, Andersson P and Erdemir A. Global energy consumption due to friction in passenger cars. *Tribol Int* 2012; 47: 221–234.
4. Johnson B and Edwards C. Exploring the pathway to high efficiency IC engines through exergy analysis of heat transfer reduction. *SAE Int J Engines* 2013; 6: 150–166.
5. Mukai K, Iijima T, Miyazaki H and Yasuhara S. The effects of design factors of the combustion chamber on heat balance in a gasoline engine. SAE technical paper 2005-01-2021, 2005.
6. Boust B, Sotton J and Bellenoue M. Unsteady heat transfer during the turbulent combustion of a lean pre-mixed methane–air flame: effect of pressure and gas dynamics. *P Combust Inst* 2007; 31: 1411–1418.
7. Labuda S, Karrer M, Sotton J and Bellenoue M. Experimental study of single-wall flame quenching at high pressures. *Combust Sci Technol* 2011; 183: 409–426.
8. Gingrich E, Ghandhi J and Reitz R. Experimental investigation of piston heat transfer in a light duty engine under conventional diesel, homogeneous charge compression ignition, and reactivity controlled compression ignition combustion regimes. *SAE Int J Engines* 2014; 7: 375–386.
9. Hendricks TL, Splitter DA and Ghandhi JB. Experimental investigation of piston heat transfer under conventional diesel and reactivity-controlled compression combustion regimes. *Int J Engine Res* 2014; 15: 684–705.
10. Dejima K, Nakabeppu O, Nakamura Y, Tsuchiya T and Nagasaka K. Three-point MEMS heat flux sensor for turbulent heat transfer measurement in internal combustion engines. *Int J Engine Res* 2019; 20: 696–705.
11. Demuyck J. *A fuel independent heat transfer correlation for premixed spark ignition engines*. Ghent: Ghent University, 2012.
12. Demuyck J, Raes N, Zuliani M, Paepe M, De Paepe M, Sierens R, et al. Local heat flux measurements in a hydrogen and methane spark ignition engine with a thermopile sensor. *Int J Hydrogen Energ* 2009; 34: 9857–9868.
13. Lejsek D and Kulzer A. Investigations on the transient wall heat transfer at start-up for SI engines with gasoline direct injection. *SAE Int J Engines* 2009; 2: 381–397.
14. Broekaert S, De Cuyper T, De Paepe M and Verhelst S. Evaluation of empirical heat transfer models for HCCI combustion in a CFR engine. *Appl Energ* 2017; 205: 1141–1150.
15. Luo X, Yu X and Jansons M. Simultaneous in-cylinder surface temperature measurements with thermocouple, laser-induced phosphorescence, and dual wavelength infrared diagnostic techniques in an optical engine. SAE technical paper 2015-01-1658, 2015.
16. Luo X, Yu X, Zha K, Jansons M and Soloiu V. In-cylinder wall temperature influence on unburned hydrocarbon emissions during transitional period in an optical engine using a laser-induced phosphorescence technique. *SAE Int J Engines* 2014; 7: 995–1002.
17. Jansons M, Lin S and Rhee KT. Infrared spectral analysis of engine preflame emission. *Int J Engine Res* 2008; 9: 215–237.
18. Someya S, Okura Y, Munakata T and Okamoto K. Instantaneous 2D imaging of temperature in an engine cylinder with flame combustion. *Int J Heat Mass Tran* 2013; 62: 382–390.
19. Nau P, Yin Z, Geigle KP and Meier W. Wall temperature measurements at elevated pressures and high temperatures in sooting flames in a gas turbine model combustor. *Appl Phys B* 2017; 123: 279.
20. Wimmer A, Pivec R and Sams T. Heat transfer to the combustion chamber and port walls of IC engines: measurement and prediction. SAE technical paper 2000-01-0568, 2000.
21. Boust B, Sotton J, Labuda SA and Bellenoue M. A thermal formulation for single-wall quenching of transient laminar flames. *Combust Flame* 2007; 149: 286–294.
22. Zhao P, Wang L and Chakraborty N. Analysis of the flame–wall interaction in premixed turbulent combustion. *J Fluid Mech* 2018; 848: 193–218.
23. Dec JE. A conceptual model of DI diesel combustion based on laser-sheet imaging.* SAE technical paper 970873, 1997.
24. Enomoto Y, Aoki Y, Emi M and Kimura S. Heat transfer coefficient on the combustion chamber wall surfaces in a naturally aspirated direct-injection diesel engine. *Int J Engine Res* 2014; 15: 606–625.
25. Mayer D, Seelig A, Kunz T, Kopple F, Mansbart M and Bargende M. Experimental investigation of flame-wall-impingement and near-wall combustion on the piston temperature of a diesel engine using instantaneous surface temperature measurements. SAE technical paper 2018-01-1782, 2018.
26. Li S-W, Kamimoto T, Kobori S and Enomoto Y. Heat transfer from impinging diesel flames to the combustion chamber wall. SAE technical paper 970896, 1997.
27. Bruneaux G. Combustion structure of free and wall-impinging diesel jets by simultaneous laser-induced fluorescence of formaldehyde, poly-aromatic hydrocarbons, and hydroxides. *Int J Engine Res* 2008; 9: 249–265.

-
28. Dec JE and Tree DR. Diffusion-flame / wall interactions in a heavy-duty DI diesel engine. SAE technical paper 2001-01-1295, 2001.
 29. Le MK, Kook S and Hawkes ER. The planar imaging of laser induced fluorescence of fuel and hydroxyl for a wall-interacting jet in a single-cylinder, automotive-size, optically accessible diesel engine. *Fuel* 2015; 140: 143–155.
 30. Pickett LM, Genzale CL, Bruneaux G, Malbec L, Hermant L, Christiansen C, et al. Comparison of diesel spray combustion in different high-temperature, high-pressure facilities. *SAE Int J Engines* 2010; 3: 156–181.
 31. Cook WJ. Determination of heat-transfer rates from transient surface temperature measurements. *AIAA J* 1970; 8: 1366–1368.
 32. Ma PC, Greene M, Sick V and Ihme M. Non-equilibrium wall-modeling for internal combustion engine simulations with wall heat transfer. *Int J Engine Res* 2017; 18: 15–25.
 33. Hendricks T and Ghandhi J. Estimation of surface heat flux in IC engines using temperature measurements: processing code effects. *SAE Int J Engines* 2012; 5: 1268–1285.
 34. Chartrand R. Numerical differentiation of noisy, non-smooth data. *ISRN Appl Math* 2011; 2011: 164564.
 35. Burgess D, Yust M and Kreider KG. Transient thermal response of plasma-sprayed zirconia measured with thin-film thermocouples. *Sensor Actuat A-Phys* 1990; 24: 155–161.
 36. Benajes J, Martín J, García A, Villalta D and Warray A. In-cylinder soot radiation heat transfer in direct-injection diesel engines. *Energ Convers Manage* 2015; 106: 414–427.
 37. Lind T, Roberts G, Eagle W, Rousselle C, Andersson I and Musculus MPB. Mechanisms of post-injection soot-reduction revealed by visible and diffused back-illumination soot extinction imaging. SAE technical paper 2018-01-0232, 2018.
 38. Payri R, García-Oliver JM, Xuan T and Bardi M. A study on diesel spray tip penetration and radial expansion under reacting conditions. *Appl Therm Eng* 2015; 90: 619–629.
 39. Tanov S, Salvador-Iborra J, Andersson Ö, Olmeda P and García A. Influence of the number of injections on piston heat rejection under low temperature combustion conditions in an optical compression-ignition engine. *Energ Convers Manage* 2017; 153: 335–345.
 40. Desantes JM, Pastor JV, García-Oliver JM and Pastor JM. A 1D model for the description of mixing-controlled reacting diesel sprays. *Combust Flame* 2009; 156: 234–249.
 41. Dahms RN, Paczko GA, Skeen SA and Pickett LM. Understanding the ignition mechanism of high-pressure spray flames. *P Combust Inst* 2017; 36: 2615–2623.